


A High-Efficiency Spectral Element Method Based on CFS-PML for GPR Numerical Simulation and Reverse Time Migration

Xun Wang , Tianxiao Yu , Deshan Feng , Siyuan Ding , Bingchao Li, Yuxin Liu, and Zheng Feng

Abstract—Improving the accuracy and efficiency of the numerical simulation of ground penetrating radar (GPR) becomes a pressing need with the rapidly increased amount of inversion data and the growing demand for migration imaging quality. In this article, we present a numerical spectral element time-domain (SETD) simulation procedure for GPR forward modeling and further apply it to the reverse time migration (RTM) with complex geoelectric models. This approach takes into account the flexibility of the finite element methods and the high precision of the spectral methods. Meanwhile, in this procedure, the complex frequency shifted perfectly matched layer (CFS-PML) is loaded to effectively suppress the echo at the truncated boundary, and the per-element GPU parallel framework used can achieve up to 5.7788 times the efficiency compared with the CPU calculation. The experiments on SETD spatial convergence and CFS-PML optimal parameter selection showed that, under the same degree of freedom, the SETD offered substantially better accuracy compared with the traditional FDTD. The experiments on RTM of different profiles with different orders of SETD via a complex geoelectric model verify the universality of the algorithm. The results indicate that the RTM imaging effect has been significantly improved with the increase of SETD order. It fully proves the great potential of efficient and high-precision SETD simulation algorithm in the RTM imaging direction and shows certain guiding significance for underground target structure exploration.

Index Terms—Complex frequency shifted perfectly matched layer (CFS-PML), ground penetrating radar (GPR), per-element GPU parallel framework, spectral element method (SEM).

I. INTRODUCTION

NUMERICAL simulation for ground penetrating radar (GPR) is an increasingly important research orientation

Manuscript received 4 October 2022; revised 22 November 2022; accepted 27 December 2022. Date of publication 4 January 2023; date of current version 16 January 2023. This work was supported in part by the National Natural Science Foundation of China (NSFC) under Grant 42104143 and Grant 42074161, in part by the Natural Science Foundation of Hunan Province under Grant 2021JJ30806 and Grant 2022JJ40584, and in part by the Fundamental Research Funds for the Central Universities of Central South University under Grant 2021zzts0270. (Corresponding author: Siyuan Ding.)

The authors are with the Key Laboratory of Metallogenic Prediction of Nonferrous Metals and Geological Environment Monitoring (Central South University), Ministry of Education, Changsha 410083, China, also with the Key Laboratory of Non-ferrous Resources and Geological Hazard Detection, Changsha 410083, China, and also with the School of Geosciences and Info-Physics, Central South University, Changsha 410083, China (e-mail: wangxun@csu.edu.cn; yutianxiaoyy@csu.edu.cn; fengdeshan@126.com; syding@csu.edu.cn; libingchao@csu.edu.cn; 8211181317@csu.edu.cn; feng_zheng@csu.edu.cn).

Digital Object Identifier 10.1109/JSTARS.2023.3234199

in computational geophysics. The analysis of the simulation of geological models can deepen the cognition degree of the GPR propagation law and reflection profile, and effectively guide the interpretation of the GPR data [1], [2]. This article intends to study a high accuracy and high efficiency numerical simulation method that can adapt to complex geological models, so as to lay a good foundation for subsequent data processing or imaging works in GPR [3], [4], [5]. In the focused time-domain approach, finite difference time-domain (FDTD) [6], [7] has some tempting advantages in GPR numerical simulation, such as wide application [8], saving storage space and computing time, and so on [9], [10], [11]. While there are two particular limitations in FDTD, 1) the choice of time-step must strictly satisfy the CFL stability condition [12], which requires a lot of computational costs, and 2) FDTD cannot be combined with the unstructured grid, making it difficult to fit complex interface. Then another forward modeling method, the finite element time-domain (FETD), is introduced into the GPR numerical simulation. Having the ability to combine with the unstructured grid, it can fit complex interfaces well [13], [14]. However, what cannot be ignored is the high computational cost required for solving large matrix linear equations, which also makes the GPU parallel acceleration difficult to be implemented. Although the concentrated mass matrix method can solve this problem, it will lead to the loss of accuracy. High-order FETD can solve the low speed and efficiency problems in the counting process of low-order FETD caused by large sparse matrices, yet it is followed by “Runge phenomenon” in high-order numerical interpolation with equidistant nodes [15], [16]. Feng [17] combined FETD and FDTD to construct a coupling algorithm to carry out GPR forward work, which adopts FETD method in the simulation region to adapt to complex structures and at the same time adopts FDTD method at the boundary to facilitate loading boundary conditions. Although it combines the advantages of FETD and FDTD, the modeling accuracy is still grid dependent. Thus, it is necessary to get a numerical simulation method that can avoid these above problems.

The spectral element method (SEM), as a numerical simulation method combining flexible finite element and spectral method [18], has been verified to have the advantages of high accuracy, high efficiency, and low memory usage. More specifically, it has the GPU acceleration capabilities and shows the higher simulation accuracy under the same degree of freedom

compared with aforementioned algorithms. SEM was first proposed and introduced into the process of solving the Navier–Stokes equations by Patera [19], which initiated the development process of SEM in the field of fluid mechanics. Priolo [20], [21] applied the Gauss–Lobatto–Chebyshev (GLC) polynomial SEM to conduct the numerical simulation of the seismic wave field. To accelerate the SEM simulation process of the seismic wave field, the parallel and domain decomposition methods were introduced by Komatitsch [22], [23], [24], [25], [26]. Until the 21st century, SEM became involved in computational electromagnetics. Lee [27], [28] proposed the SEM procedure based on the mixed order Gauss–Lobatto–Legendre (GLL) basis function to solve the electromagnetic waveguide problem, which proved the superiority of SEM compared with the traditional FEM in the vector field. Unlike computational electromagnetics, geophysical electromagnetics typically targets large-scale geological models, SEM was rarely used to carry out numerical simulation in geophysics, therefore. With the assistance of SEM based on GLL polynomials, Huang [29] greatly improved the efficiency and accuracy of the airborne electromagnetic frequency-domain and time-domain numerical simulation. The SEM research in the aspect of GPR is even less. To simulate nonuniform geological models better, SETD is applied to GPR numerical simulation based on the Matlab programming platform by Zarei [30], proving the high efficiency and accuracy of SETD compared with the traditional FETD. However, the absorption boundary used in this research is the first-order Clayton and Engquist absorption boundary condition (CE-ABC) proposed by Clayton and Engquist [31], which has a weakness that the absorptive capacity of CE-ABC is restricted by the angle of incidence and the distance between the target and the boundary. Obviously, an excellent absorption boundary is extremely requisite.

As is well known, the perfectly matched layer (PML), proposed by Berenger [32] in 1994, is a milestone in the absorption boundary history. However, the theory of PML does not follow Maxwell’s equations and its physical mechanism is fuzzy. In addition, the calculation of electromagnetic field splitting [33], [34] based on PML boundary condition increases the computational cost and difficulties of numerical implementation. Besides, PML has a poor ability on absorbing low-frequency wave, grazing angle wave, and evanescent wave with small incident angles [35], [36]. In order to accelerate the calculation process, reduce the difficulties, and improve the absorption ability of PML boundary condition, Kuzuoglu and Mittra [37] proposed the CFS-PML technique. Shortly afterward, Berenger [38], [39], [40] carried out a series of application research about the absorption ability of CFS-PML in wave conduction problems and proved the superiority compared with traditional PML, hence CFS-PML was used widely in the days that followed. Masoud and Abdolali [41], [42] applied CFS-PML to the vector FETD simulation of the Maxwell equations, which is derived by convolution under the first-order equation. Feng [13] also derived the equation of CFS-PML by convolution except the process was under the second-order Maxwell equations, and introduced it into the second-order vector FETD. Nonetheless, the convolutional process with the second-order Maxwell equations is complicated and unintelligible. To avoid that problem,

the auxiliary differential equation (ADE) strategy [43], [44] is an excellent alternative to the convolutional process.

In order to give full play to the advantages of SEM and realize high-accuracy numerical simulation of various complex models, we will apply SETD into GPR numerical simulation, and CFS-PML, which can absorb low-frequency wave, grazing angle wave, and evanescent wave with small incident angles better, will be introduced as the absorption boundary. To derive and calculate the governing equation of CFS-PML in the time domain more easily, we will put ADE strategy to use. The GPU per-element parallel framework will be applied to improve the efficiency and accelerate the simulation process. An efficient and fast forward modeling can assist a series of work, such as the high-precision reverse time migration (RTM) imaging of GPR. With the deepening of detection requirements, the imaging for GPR data is faced with complex terrain environments and is still a technical challenge. Several attempts can be made to improve the accuracy of the RTM with the complex geologies, especially with the irregular interface. From the perspective of GPR data processing, Song and Xiang [45], [46] proposed a new clutter suppression method, which can ensure the accuracy of antipersonnel mine detection and reduce the false alarm rate of detection in a strong clutter environment. In another aspect, Bradford [47] used terrain correction to improve RTM imaging results when faced with the problem of complex terrain. In this article, taking a different attempt to improve the RTM imaging quality under complex terrain, we improve the efficiency and accuracy of the forward modeling via our SETD framework. In this regard, the results of different orders of RTM will be the powerful evidence to verify the great potential of SETD in the aspect of RTM imaging [48].

The rest of this article is organized as follows: In Section II, we derive the ADE CFS-PML governing equation, and provide the related concepts of SEM, then the matrix representation of SETD and the GPU parallel framework is presented. In Section III, we carry out an optimal parameter selection experiment of CFS-PML. Next, in Section IV, we analyze the spatial convergence of SETD. In Section V, we present the SETD simulation results of a complex geoelectric model. Then, based on the simulation results, the RTM imaging results are presented. Then, the accuracy, high efficiency, and strong practicability of SETD algorithm are tested. Finally, Section VI concludes this article.

II. CFS-PML-BASED PER-ELEMENT PARALLEL SETD

A. Complex Frequency Shifted Perfectly Matched Layer

According to the Maxwell’s electromagnetism theory [49], 2-D TM wave (E_z, H_x, H_y) has the following form:

$$-\frac{\partial}{\partial x} \left(\frac{1}{\mu} \frac{s_y}{s_x} \frac{\partial E_z}{\partial x} \right) - \frac{\partial}{\partial y} \left(\frac{1}{\mu} \frac{s_x}{s_y} \frac{\partial E_z}{\partial y} \right) - \omega^2 \varepsilon s_x s_y E_z = -j\omega J_z \quad (1)$$

where E is the electric intensity (V/m), μ is the permeability, and ε is the permittivity. The coordinate-stretched factor s_i of

CFS-PML proposed by Kuzuoglu and Mittra [37] is

$$s_i = \kappa_i + \frac{\sigma_i}{a_i + j\omega\varepsilon_0} = \kappa_i + \frac{\beta_i}{\alpha_i + j\omega}, \frac{\sigma_i}{\varepsilon_0} \rightarrow \beta_i, \frac{a_i}{\varepsilon_0} \rightarrow \alpha_i \quad (2)$$

where σ_i is the conductivity in direction i of the PML layer, the introduction of κ_i and α_i is to improve the absorption ability of these evanescent wave and low-frequency wave, here $i = x, y, z$.

Substitute (2) into (1), this expression can be simplified to

$$-\frac{\partial}{\partial x} \left(\frac{1}{\mu} \frac{\kappa_y}{\kappa_x} \frac{\partial E_z}{\partial x} \right) - \frac{\partial}{\partial y} \left(\frac{1}{\mu} \frac{\kappa_x}{\kappa_y} \frac{\partial E_z}{\partial y} \right) - \omega^2 \varepsilon \kappa_x \kappa_y E_z + j\omega \varepsilon H_1 E_z + \varepsilon H_2 E_z + f = -j\omega J_z \quad (3)$$

where

$$H_1 = \kappa_y \beta_x + \kappa_x \beta_y, H_2 = \beta_x \beta_y - \kappa_y \alpha_x \beta_x - \kappa_x \alpha_y \beta_y, \\ f = -\frac{\partial}{\partial x} \left(\frac{1}{\mu} P_{1x} - \frac{1}{\mu} P_{2x} \right) - \frac{\partial}{\partial y} \left(\frac{1}{\mu} P_{1y} - \frac{1}{\mu} P_{2y} \right) + Q_x + Q_y. \quad (4)$$

Transform (3) into time domain and sort out

$$-\frac{\partial}{\partial x} \left(\frac{1}{\mu} \frac{\kappa_y}{\kappa_x} \frac{\partial E_z}{\partial x} \right) - \frac{\partial}{\partial y} \left(\frac{1}{\mu} \frac{\kappa_x}{\kappa_y} \frac{\partial E_z}{\partial y} \right) + \varepsilon \kappa_x \kappa_y \frac{\partial^2 E_z}{\partial t^2} + \varepsilon H_1 \frac{\partial E_z}{\partial t} + \varepsilon H_2 E_z + f = -\frac{\partial J_z}{\partial t} \quad (5)$$

where different values of κ and α correspond to different absorption effects. When κ is given no specific value and $\alpha = 0$, we get $s_i = \kappa_i + \sigma_i/j\omega\varepsilon_0$, $i = x, y, z$. Put this formula to deduce the time domain equation, the results are as follows:

$$\begin{cases} -\frac{\kappa_y}{\mu\kappa_x} \frac{\partial^2 E_z}{\partial x^2} - \frac{\kappa_x}{\mu\kappa_y} \frac{\partial^2 E_z}{\partial y^2} - \frac{1}{\mu} \left(\frac{\partial P}{\partial x} + \frac{\partial Q}{\partial y} \right) \\ + \varepsilon \kappa_x \kappa_y \frac{\partial^2 E_z}{\partial t^2} + (\kappa_x \sigma_y + \kappa_y \sigma_x) \frac{\partial E_z}{\partial t} + \frac{\sigma_x \sigma_y}{\varepsilon_0^2} E_z = -\frac{\partial J_z}{\partial t} \\ \frac{\partial P}{\partial t} + \frac{\sigma_x}{\varepsilon_0 \kappa_x} P = \frac{\kappa_x \sigma_y - \kappa_y \sigma_x}{\varepsilon_0 \kappa_x^2} \frac{\partial E_z}{\partial x} \\ \frac{\partial Q}{\partial t} + \frac{\sigma_y}{\varepsilon_0 \kappa_y} Q = \frac{\kappa_y \sigma_x - \kappa_x \sigma_y}{\varepsilon_0 \kappa_y^2} \frac{\partial E_z}{\partial y}. \end{cases} \quad (6)$$

The derivation process is greatly simplified and the number of auxiliary variables is reduced compared with the variables adopted by the ADE strategy in the Appendix. However, the absorption ability of low-frequency wave is neglected to some extent. To strike an appropriate balance between the calculation cost and absorption ability, the discussion on the value of α is requisite and it will be expanded later.

The selection of CFS-PML parameters is given by the following formula [13]:

$$\sigma = \sigma_{\max} \left(\frac{\rho}{d} \right)^m, \sigma_{\max} = -\frac{(m+1)c_0\varepsilon_0 \ln R}{2d\sqrt{\varepsilon}}, \\ \kappa = 1 + (\kappa_{\max} - 1) \left(\frac{\rho}{d} \right)^m, \alpha = \alpha_0 \left[1 - \left(\frac{\rho}{d} \right)^m \right] \quad (7)$$

where d is the thickness of the absorbing boundary, ρ is the distance from center of element to simulation region, and κ_{\max} is the maximum value of parameter κ . The selection of reflection coefficient R , exponential order m , κ_{\max} , and α_0 has an important influence on the absorption effect.

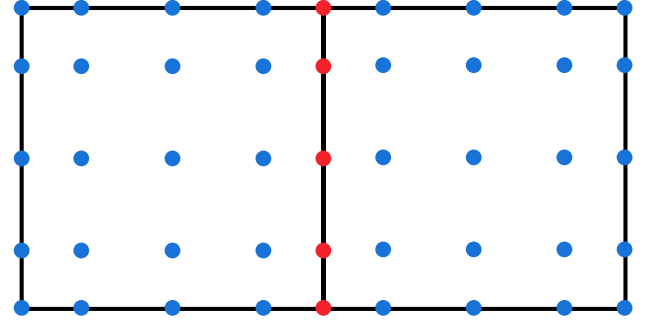


Fig. 1. Distribution diagram of spectral element nodes of order $P = 4$.

B. Time-Domain Spectral Element Method

SETD has two main differences compared with FETD as follows [50], [51], [52]: 1) The high-order Lagrange polynomial is used to construct the interpolation basis function. Because of their orthogonality, the mass matrix and damping matrix constructed are single diagonal matrices, which greatly reduces the calculation cost, improves the integration efficiency, and the linear equations can be directly inverted to solve. 2) The interpolation nodes are anomalous, which is different from the traditional high-order FETD with equidistant nodes. SETD uses GLL nodes which have been proven to have high interpolation accuracy and robustness. Because of the irregularity of its distribution, the ‘‘Runge phenomenon’’ is effectively avoided and the interpolation accuracy is greatly improved.

First of all, usually, we divide the simulation region into a series of nonoverlapping small elements and configure GLL nodes in each element. Fig. 1 shows the distribution mode of GLL nodes of two elements in the case of order 4. Grid nodes are distributed in the element interior, edge, and corner, and tend to distribute at both ends of the same edge. This irregular distribution mode significantly weakens the ‘‘Runge phenomenon’’ and has high interpolation accuracy.

As mentioned above, the high-order Lagrange polynomial is used to construct the interpolation basis function on the GLL nodes. The 2-D form of the Lagrange interpolation polynomial with order 4 is as follows [53]:

$$f(x, y) \approx P_f(x, y) = \sum_{i,j=1}^4 f(x_i, y_j) N_i(x) N_j(y) \quad (8)$$

$$N_1(\xi) = \frac{(\xi - \xi_2)(\xi - \xi_3)(\xi - \xi_4)}{(\xi_1 - \xi_2)(\xi_1 - \xi_3)(\xi_1 - \xi_4)}, \dots \\ N_4(\xi) = \frac{(\xi - \xi_2)(\xi - \xi_3)(\xi - \xi_4)}{(\xi_4 - \xi_2)(\xi_4 - \xi_3)(\xi_4 - \xi_4)} \quad (9)$$

where N_i and N_j are the shape functions. Therefore, we derive the weak solution form by the Galerkin weighted residual method, and then we obtain the linear equations for the next step.

However, for the complex-surface model, simply using the rectangular element, as shown in Fig. 1 may cause a huge error. To decrease the error, we directly define the model characteristics on the GLL nodes, and build an unstructured grid to fit the complex-surface of the model, as shown in Fig. 2 as follows.

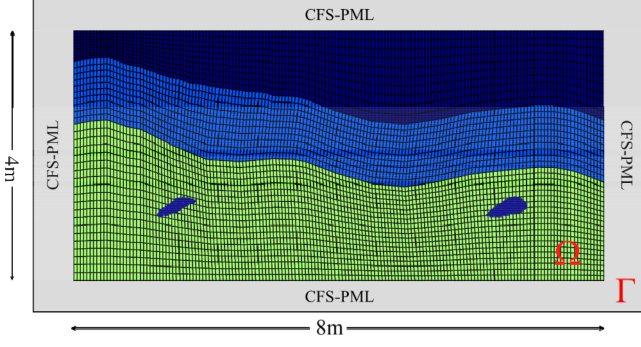


Fig. 2. Grid generation diagram of complex geoelectric model.

In conjunction with the above, we obtain the weak solution by the Galerkin weighted residual method under this complex-surface model building pattern.

According to the Galerkin method mentioned above, the weak solution form can be derived by multiplying both ends of (5) by a test function and integrating in the whole simulation region

$$\begin{aligned} \iint_{\Omega} \frac{\partial J_z}{\partial t} v d\Omega &= \int_{\Gamma} \frac{\partial}{\partial x} \left(\frac{1}{\mu} \frac{\kappa_y}{\kappa_x} \frac{\partial E_z}{\partial x} + \frac{1}{\mu} P_{1x} - \frac{1}{\mu} P_{2x} \right) v d\Gamma \\ &+ \int_{\Gamma} \frac{\partial}{\partial y} \left(\frac{1}{\mu} \frac{\kappa_x}{\kappa_y} \frac{\partial E_z}{\partial y} + \frac{1}{\mu} P_{1y} - \frac{1}{\mu} P_{2y} \right) v d\Gamma \\ &- \iint_{\Omega} (Q_x + Q_y) v d\Omega - \varepsilon \kappa_x \kappa_y \iint_{\Omega} \frac{\partial^2 E_z}{\partial t^2} v d\Omega \\ &- \varepsilon H_1 \iint_{\Omega} \frac{\partial E_z}{\partial t} v d\Omega - \varepsilon H_2 \iint_{\Omega} E_z v d\Omega \end{aligned} \quad (10)$$

where Γ and Ω are the boundary region and the model region, respectively, and v is the trial function. We adopt the Dirichlet boundary condition with a displacement of 0 on the PML, and then the spectral element equation corresponding to (10) can be deduced by the Galerkin method as follows:

$$M \ddot{E}_z + M_1 \dot{E}_z + K E_z + F = 0 \quad (11)$$

$$F = C (Q_x + Q_y) + f - K_x (P_{1x} - P_{2x}) - K_y (P_{1y} - P_{2y}) \quad (12)$$

where \ddot{E}_z , \dot{E}_z , \dot{P}_{1x} , \dot{P}_{2x} , \dot{P}_{1y} , \dot{P}_{2y} , \dot{Q}_x , and \dot{Q}_y are the quadratic and primary derivatives of E_z , P_{1x} , P_{2x} , P_{1y} , P_{2y} , \dot{Q}_x , and \dot{Q}_y concerning time t , the expressions of these coefficient matrices, respectively, are as follows, and where N is the shape function taken in the whole region

$$\begin{cases} M = \iint_{\Omega} \varepsilon \kappa_x \kappa_y N N^T d\Omega, M_1 = \iint_{\Omega} \varepsilon H_1 N N^T d\Omega \\ K = \iint_{\Omega} \left[\varepsilon H_2 N N^T - \frac{1}{\mu} \left(\frac{\kappa_y}{\kappa_x} \frac{\partial N}{\partial x} \frac{\partial N^T}{\partial x} + \frac{\kappa_x}{\kappa_y} \frac{\partial N}{\partial y} \frac{\partial N^T}{\partial y} \right) \right] d\Omega \\ C = \iint_{\Omega} N N^T d\Omega, f = \iint_{\Omega} \frac{\partial J_z}{\partial t} N N^T d\Omega \\ K_x = \frac{1}{\mu} \iint_{\Omega} \frac{\partial N}{\partial x} N^T d\Omega, K_y = \frac{1}{\mu} \iint_{\Omega} \frac{\partial N}{\partial y} N^T d\Omega. \end{cases} \quad (13)$$

For the time domain, we adopt the central-difference time discrete method to solve (12) and (13). The first and second derivatives in the equation can be approximated by the following

equation:

$$\begin{aligned} \dot{E}_z^n &= \frac{1}{2\Delta t} [E_z^{n+1} - E_z^{n-1}] \\ \ddot{E}_z^n &= \frac{1}{(\Delta t)^2} [E_z^{n+1} - 2E_z^n + E_z^{n-1}]. \end{aligned} \quad (14)$$

Substitute (14) into (12) and (13) to obtain the time discrete equation

$$\begin{aligned} \left(\frac{M}{\Delta t^2} + \frac{M_1}{2\Delta t} \right) E_z^{n+1} + \left(K - \frac{2M}{\Delta t^2} \right) E_z^n \\ + \left(\frac{M}{\Delta t^2} - \frac{M_1}{2\Delta t} \right) E_z^{n-1} + F = 0 \end{aligned} \quad (15)$$

$$\begin{aligned} F &= C (Q_x^n + Q_y^n) + f_n \\ &- K_x (P_{1x}^n - P_{2x}^n) - K_y (P_{1y}^n - P_{2y}^n) \end{aligned} \quad (16)$$

where n is the number of time steps and Δt is the time step.

As mentioned at the beginning of Section II-B, we directly inverse (16) to obtain the E_z at each moment as the time step progresses. However, in the traditional FEM, (16) cannot be directly solved by inverse because of the large sparse coefficient matrices. For this problem, the centralized mass matrix technique works but gives up the advantage of parallel computing. In this regard, SETD can carry out parallel computation while constructing diagonal mass and damping matrix. On this basis, a parallel framework of GPU per-element can be constructed to accelerate the numerical simulation of GPR.

C. GPU Per-Element Parallel SETD Framework

Due to the limitation of the physical memory of personal microcomputers and the demand for high efficiency of simulation processing, how to reduce the memory consumption and improve the efficiency of SETD forward computing becomes the focal point. The diagonal mass and damping matrix formed in SETD lay a foundation for the feasibility of parallel calculation. Therefore, we propose a GPU parallel framework [54].

The device architecture of GPU is different from that of CPU. GPU has more computing units and parallel features. Therefore, GPU has obvious advantages in floating point and matrix calculation. In order to improve the efficiency of SETD, GPU parallel strategy is adopted in the single source simulation of the 2-D GPR wave field. We present the algorithm flow chart in the Fig. 3.

As can be seen in the Fig. 3, in the 2-D SETD algorithm using GPU parallelism, the field value is initialized by CPU first, and then allocated to GPU, which is accessed by global memory. After initialization, the calculation module of each field value is realized by calling the GPU Kernel program: when it comes to (12), the coefficient matrices M , M_1 , and F are diagonal matrices, so that the calculation process of $M E_z$ and $M_1 E_z$ is low-cost and quick. While K , K_x , and K_y are sparse matrices with partial derivative terms, the main calculation cost lies in the calculation process of $K E_z$, $K_x (P_{1x} - P_{2x})$, and $K_y (P_{1y} - P_{2y})$. Therefore, we divide this calculation process into two successive parts as follows: 1) First, the first-order and second-order partial

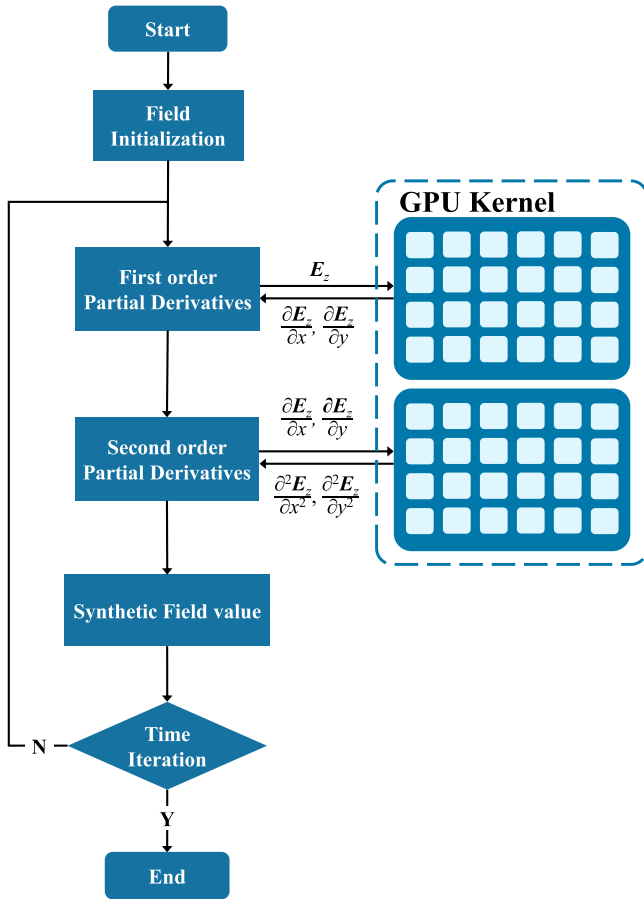


Fig. 3. Diagram of GPU-SETD algorithm flow.

derivatives of the field value E_z in the x and y directions of each element in the Kernel are, respectively, obtained. 2) On this basis, the auxiliary fields P , Q , and E_z are calculated. The calculation of all elements in the Kernel is performed in parallel and iterated continuously until a given time.

In order to achieve higher computational efficiency, the per-element technique is combined in the step of solving the field value. That is, the coefficient matrix is solved on a single spectral element and then the field value is directly solved before the whole assembly. Compared with the global coefficient matrix is synthesized first and then solved in the traditional FETD, per-element technique effectively avoids the formation of large sparse matrices and does not require large-scale matrix calculation. We greatly reduce the computational cost and programming difficulty through the combination of per-element technique and GPU parallelism.

We establish a 2-D simple model without absorption boundary to compare computing performance between the per-element GPU parallel algorithm and CPU serial algorithm. Test calculations are performed on NVIDIA GeForce GTX 1660 Ti GPU and Intel(R) Core(TM) I7-11700F CPU. We set the source at the center of the model and present Fig. 4 of the running time and speed-up ratio of per-element GPU parallel algorithm and CPU serial algorithm in 501 time steps at different orders.

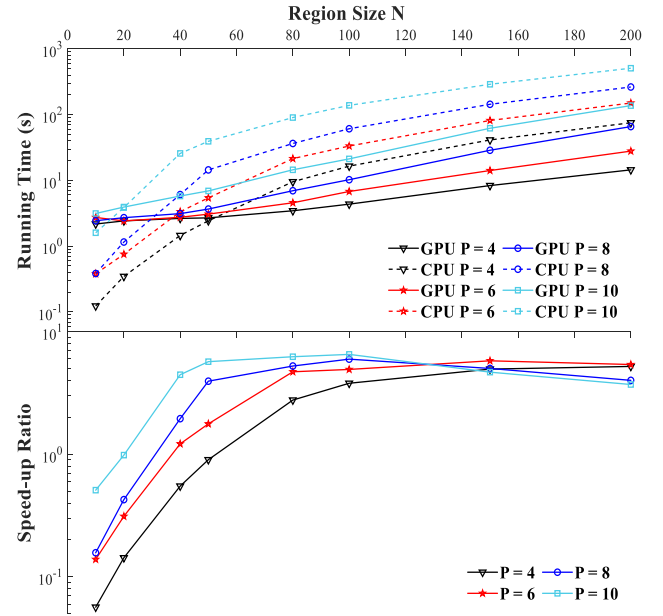


Fig. 4. Running time and speed-up ratio diagram of per-element GPU parallel algorithm and CPU serial algorithm after 501 time-steps at different orders.

TABLE I
COMPUTING TIME OF GPU AND CPU (501 TIME STEPS)

Region (N × N)	GPU running-time (s)	CPU running-time (s)	Speed-up ratio
10×10	2.7304	0.3789	0.1388
20×20	2.4169	0.7526	0.3114
40×40	2.7476	3.3381	1.2149
50×50	3.0666	5.4221	1.7681
80×80	4.5613	21.4494	4.7025
100×100	6.7821	33.3329	4.9148
150×150	14.1221	81.6081	5.7788
200×200	27.8898	150.3464	5.3907

In Fig. 4, the running time curve trend of GPU parallel program and CPU serial program is the same, and the speed-up ratio of the four orders reaches the maximum when the region size is 150×150 . According to the image, we select $P = 6$ and sort out Table I of the running time and speed-up ratio of the two methods.

As can be seen from the comprehensive chart, in the 10×10 grid, the computing time of GPU parallel program is longer than that of the 20×20 grid. This is because in a small scale grid, the computation time of the CPU serial program is actually less, and the data transfer time takes a larger proportion, which reduces the calculation ratio of the program. It also shows that GPU cannot play its advantage of matrix calculation in small-scale grids. When the size $N \times N$ gradually increases, especially exceeding 80×80 , the acceleration ratio increases significantly. In this case, the GPU parallel algorithm has an obvious advantage over the CPU serial program in terms of computing time. When the region size reaches 200×200 , the acceleration ratio decreases compared to 150×150 , indicating that the physical memory

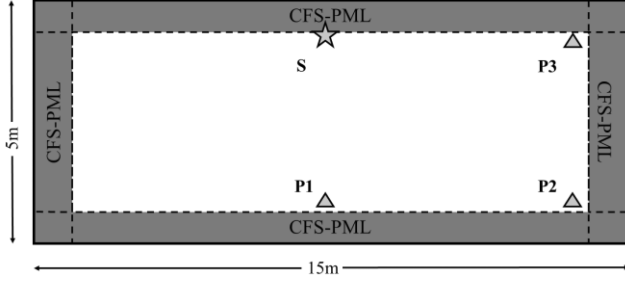


Fig. 5. Diagram of narrow and long simple model.

of the computer is gradually saturated, and the computer itself cannot bear the larger grid calculation.

We run a series of analyses of the chart above: the computation time of 20×20 of the GPU parallel algorithm is longer than that in 10×10 . The running time of the CPU serial algorithm is actually less since the data transmission time between GPU and CPU accounts for a larger proportion in the small grid scale, the computing performance only accounts for a pinging proportion, which fully shows that GPU cannot play its advantage in matrix operation in small grid scale. With the region size N increasing gradually, especially when the region size exceeds 80×80 , the speed-up ratio increases significantly. At this region size, the GPU parallel algorithm has obvious advantages over the CPU serial program in terms of running time. When the region size reaches 200×200 , the speed-up ratio decreases compared with 150×150 , indicating that the physical memory of the computer is gradually saturated. With a large number of SETD nodes, the computer itself cannot afford to perform larger grid computations. However, the contribution of too many SETD nodes to the simulation accuracy is wasted.

In summary, the GPU per-element-parallel strategy proposed in this article is feasible and can reduce the computing time to a large extent, laying a foundation for efficient SETD numerical simulation.

III. CFS-PML PARAMETER SELECTION EXPERIMENT

In order to maximize the absorption effect of CFS-PML, we establish a narrow and long model to carry out the experiment of the optimal absorption parameters and test the influence of various parameters on the absorption effect.

The numerical model is 15.0×5.0 m, and we divide it into 30×10 rectangular elements with spacing of 0.5 m and the number of absorption layer is 2. The permittivity ϵ of the model is 3.0, and the excitation source is located at the center of the upper surface. A 100+MHz zero-phase Ricker wavelet is adopted. The sampling interval is calculated according to CFL stability conditions. The positions of observation points P1, P2, and P3 are shown in Fig. 5.

The received signal E_S and reference model signal E_{ref} at observation points are obtained by expanding the model by four times, and $E_{ref_{max}}$ of the reference model signal with the largest amplitude is obtained, and the reflection error is calculated by the following formula:

$$\text{Error}_{db} = 20 \times \log(|E_S - E_{ref}|/|E_{ref_{max}}|). \quad (17)$$

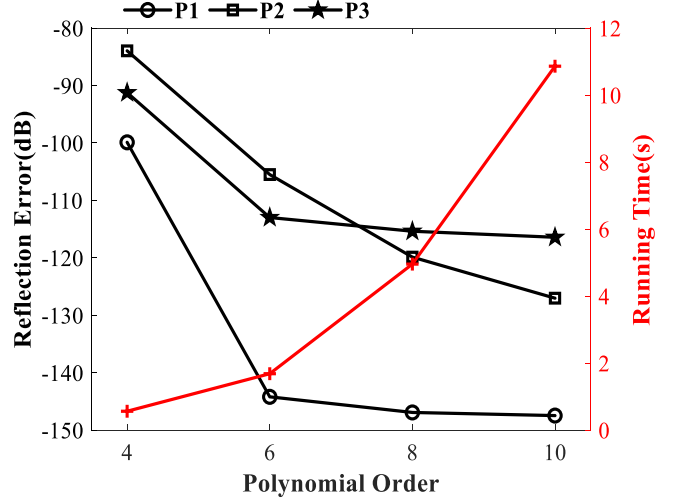


Fig. 6. Maximum reflection error distribution diagram of polynomial order.

TABLE II
OPTIMAL PARAMETER SELECTION OF CFS-PML WITH DIFFERENT ORDERS

P	m	R	κ_{max}	α_0
4	2	10^{-3}	1	1.5
6	3	10^{-4}	3	2
8	4	10^{-4}	4	1
10	5	10^{-4}	4	0.5

First, the maximum reflection error experiment of different observation points with different orders is carried out, and we present the maximum reflection error distribution diagram in Fig. 6. By analyzing Fig. 6, it can be seen that the higher the order, the smaller the reflection error will be, but the calculation time and cost will increase greatly. Taking these two factors into consideration, order $P = 6$ with a smaller reflection error and lower calculation cost is chosen as an example.

Taking order $P = 6$ as an example, Fig. 7 shows the maximum reflection error distribution of different parameters m and reflection coefficient R at different observation points. By analyzing Fig. 7, it can be seen that the reflection error reaches the minimum at observation points P1, P2, and P3 when $m = 3$, $R = 1 \times 10^{-4}$.

We select $m = 3$, $R = 1 \times 10^{-4}$ to experiment with the influence of κ_{max} on the reflection error. The model and detection points are set the same as above, and the reflection error distribution of parameter κ_{max} at observation points P1, P2, and P3 are shown in Fig. 8(Black-Line). By analyzing the reflection error distribution of κ_{max} at observation points P1, P2, and P3, the reflection error reached the minimum when $\kappa_{max} = 3$. Therefore, we set $m = 3$, $R = 1 \times 10^{-4}$, $\kappa_{max} = 3$, and the influence of parameter α_0 on the reflection error is analyzed. The reflection error distribution of α_0 at observation points P1, P2, and P3 are shown in Fig. 8(Red-Line), it can be seen that the reflection error reached the minimum when $\alpha_0 = 2$.

The order P is, respectively, set as 4, 6, 8, and 10 to carry out the optimal parameter selection experiment above, and the parameter selections are sorted out, as shown in Table II.

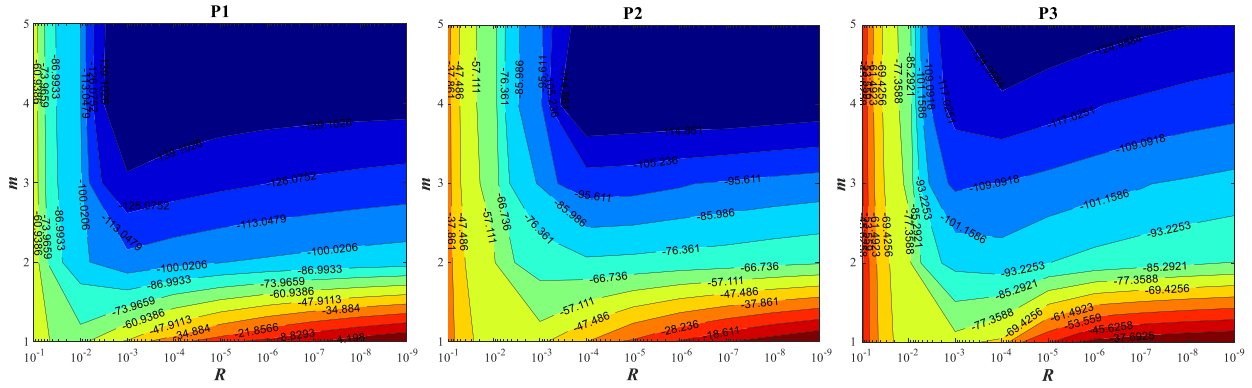


Fig. 7. Maximum reflection error distribution diagram of the parameters m and the reflection coefficient R .

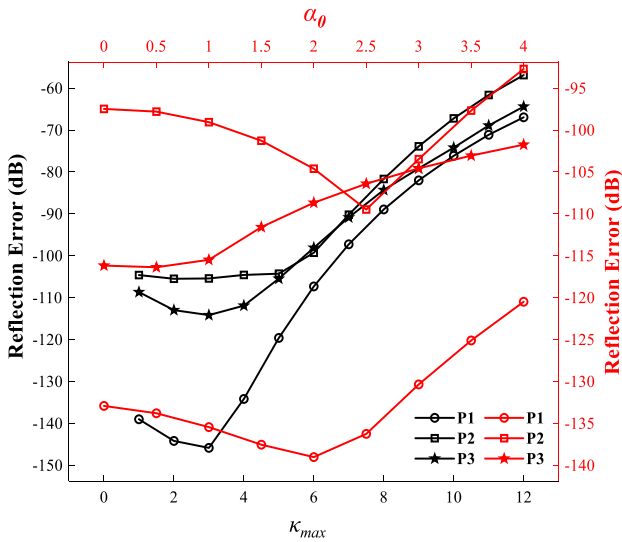


Fig. 8. Maximum reflection error distribution diagram of κ_{max} and α_0 .

In fact, when the order P goes higher, such as 8 or 10, there is only a slight difference between taking $\alpha_0 = 0$ and taking the best α_0 to compare the maximum reflection error. Therefore, in the case of higher order, setting $\alpha_0 = 0$ can simplify the derivation process of the formula, save the calculation cost, and have satisfactory accuracy.

Another important parameter affecting the absorption effect of CFS-PML is the number of the layer. In the optimal parameter selection experiment, we only set the CFS-PML layer number as 2, and the absorption effect at the truncated boundary can already meet the requirements. However, in FETD, it is usually necessary to set the CFS-PML layer number to 20 to achieve a better absorption effect. In this respect, SETD only needs fewer PML layers to achieve a better absorption effect, and as the order increases, fewer PML layers are required, which has distinct advantages over FETD.

IV. ANALYSIS OF SPATIAL CONVERGENCE OF SETD

As mentioned above, the time discretization method adopts the central difference, which only has the second-order convergence, therefore we carry out the convergence analysis

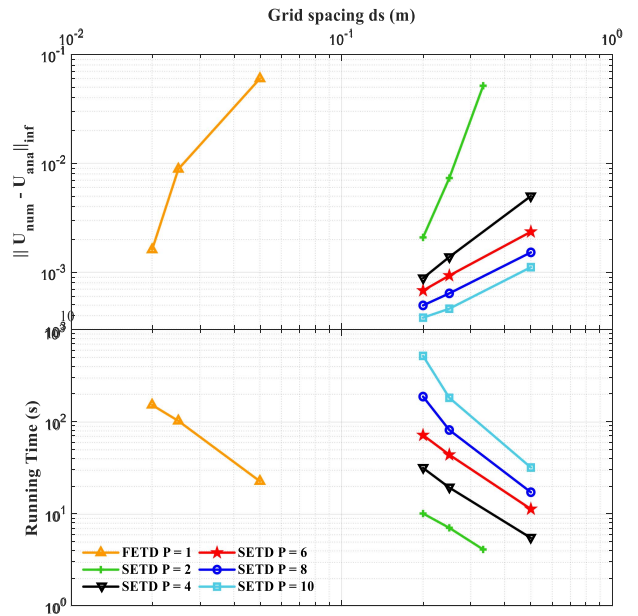


Fig. 9. Error and running time diagram of P and ds .

only for the spatial-step ds . In order to study the influence of ds and order P on SETD, a simple model with the source at the center is established to conduct a convergence analysis experiment, and the infinite norm of the numerical and analytical solution at the receiving point is used as the convergence evaluation criteria. The experimental process is as follows.

The receiver is located 0.5 m to the right of the excitation source. To avoid the irrelevant variable dt , that meets CFL conditions in all cases is selected. Set the order P as 2, 4, 6, 8, and 10, and a fine grid FETD experiment result is added for comparison. SETD ds is set as 0.2, 0.25, and 0.5 m, and FETD as 0.02, 0.025, and 0.05 m. We present the diagram of the error and running time of the algorithm in Fig. 9.

The corresponding ds of the three points from left to right of each curve is (1), (2), and (3), respectively, and the relationship between order P , ds , and degrees of freedom is shown as Table III.

In this experiment, when order $P = 2$, the error obtained by using ds of the same order as other ds is too large, so separately set ds as 0.2, 0.25, 0.33 m. It can be seen from the comprehensive

TABLE III
CORRESPONDING RELATIONSHIPS BETWEEN DIFFERENT ORDERS, ds AND DEGREES OF FREEDOM

Order P	$ds = (1)$	$ds = (2)$	$ds = (3)$
FETD	292681	194481	58081
P = 2	10201	6561	3721
P = 4	40401	25921	6561
P = 6	90601	58081	14641
P = 8	160801	103041	25921
P = 10	251001	160801	40401

The bold entities are intended to highlight the process of comparing the FETD and SETD with the same degree of freedom.

Fig. 9 and Table III that SETD and FETD are off by an order of magnitude on ds , even the order $P = 2$ SETD, which is the most similar, has obvious advantages in terms of running time. Moreover, the degree of freedom of order $P = 2$ SETD is much smaller than that of FETD. Although the running time of order $P = 10$ SETD is longer, its accuracy is several levels of magnitude higher than FETD, which even generally has higher degrees of freedom than SETD. After the above analysis, the following conclusions can be drawn.

- 1) In the case of the same degree of freedom, although the calculation time of SETD is slightly longer, its accuracy is multiple differences, and SETD does not need a high degree of freedom to achieve high accuracy.
- 2) In the case of the same precision, it is obvious that the calculation time of SETD is much less than that of FETD, and SETD only needs less time to achieve the same precision as FETD.
- 3) In the case of the same calculation time, the accuracy of SETD is much higher than that of FETD. Compared with FETD, SETD can achieve higher accuracy in a limited time.

For SETD itself, through the experiment found that the space convergence is not only related to ds but also related to the way of time dispersion, because the central difference discrete method has second-order convergence, improving SETD order does not accelerate its convergence speed. Therefore, a much higher order of time discrete methods, such as low memory Runge–Kutta method is required with the next work.

V. EXAMPLE AND APPLICATION OF SETD GPR SIMULATION

In order to better explain the simulation result of GPR SETD, a GPU per-element parallel SETD simulation algorithm based on CFS-PML is written on the Matlab platform. The complex model of the undulating surface, as shown in Fig. 10, is established, and the radar antenna is measured along the undulating surface. The permittivity of the uppermost layer is 1.0. There are three lithologic units in the first layer, whose permittivity is 5.0, 7.0, and 9.0, respectively, from left to right. The permittivity of the lower layer is 11.0, and the permittivity of both irregular cavities is set to 1.0. Considering that the two data acquisition methods of profile method and wide-angle method are often used in 2-D GPR detection, the numerical simulation of the complex

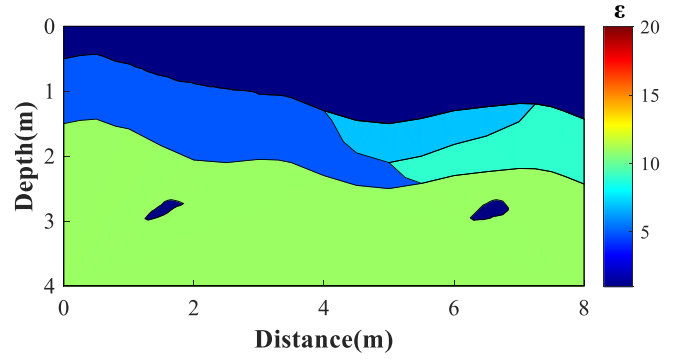


Fig. 10. Diagram of undulating surface geoelectric model.

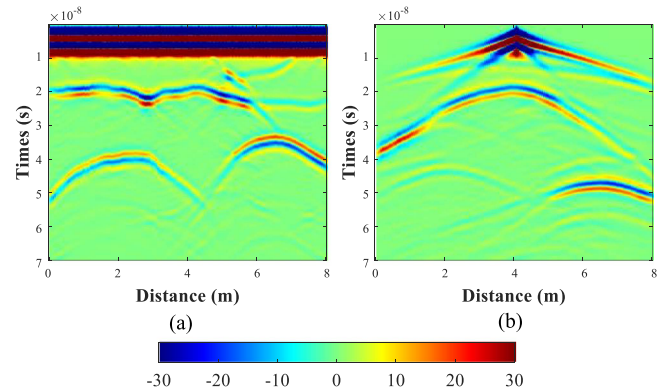


Fig. 11. Simulation results of GPR to undulating surface geoelectric model. (a) Profile method. (b) Wide-angle method.

GPR model is carried out based on the profile method and wide-angle method with the order $P = 6$ SETD as an example.

The profile method adopts the mode of self-excitation and self-receiving, moving synchronously from left to right along the undulating surface. The dt is determined according to CFL stability condition, and the time window length is 70 ns. The excitation source is a 200-MHz zero-phase Ricker wavelet, and the radar antenna is 0.1-m away from the ground surface. The outer boundary of the simulated region is CFS-PML with $m = 3$, $R = 1 \times 10^{-4}$, $\kappa_{\max} = 3$, $\alpha_0 = 2$, and the number of layers is 4. Fig. 11 shows the radar profile of 165 waveforms obtained by the SETD algorithm.

As can be seen from Fig. 11(a), the truncation effect of CFS-PML on the boundary is relatively ideal, and there is no interference with the artificial truncation boundary in the forward profile. At the depth of about 20 ns, the underground undulation interface can be identified from the reflected waves. The shape and position of the undulation interface are also clearly discernible in the profile. However, due to the existence of the undulating surface, topographic correction is required to obtain its true shape. The reflection interface of two lithologic units can be seen on the right, and the permittivity of the right lithological unit differs little from the permittivity of underground media, so the reflected wave is not obvious in comparison. The hyperbolic diffraction waves are also observed at the depth of 40 ns in these two irregular cavities. The hyperbolic shape is deformed

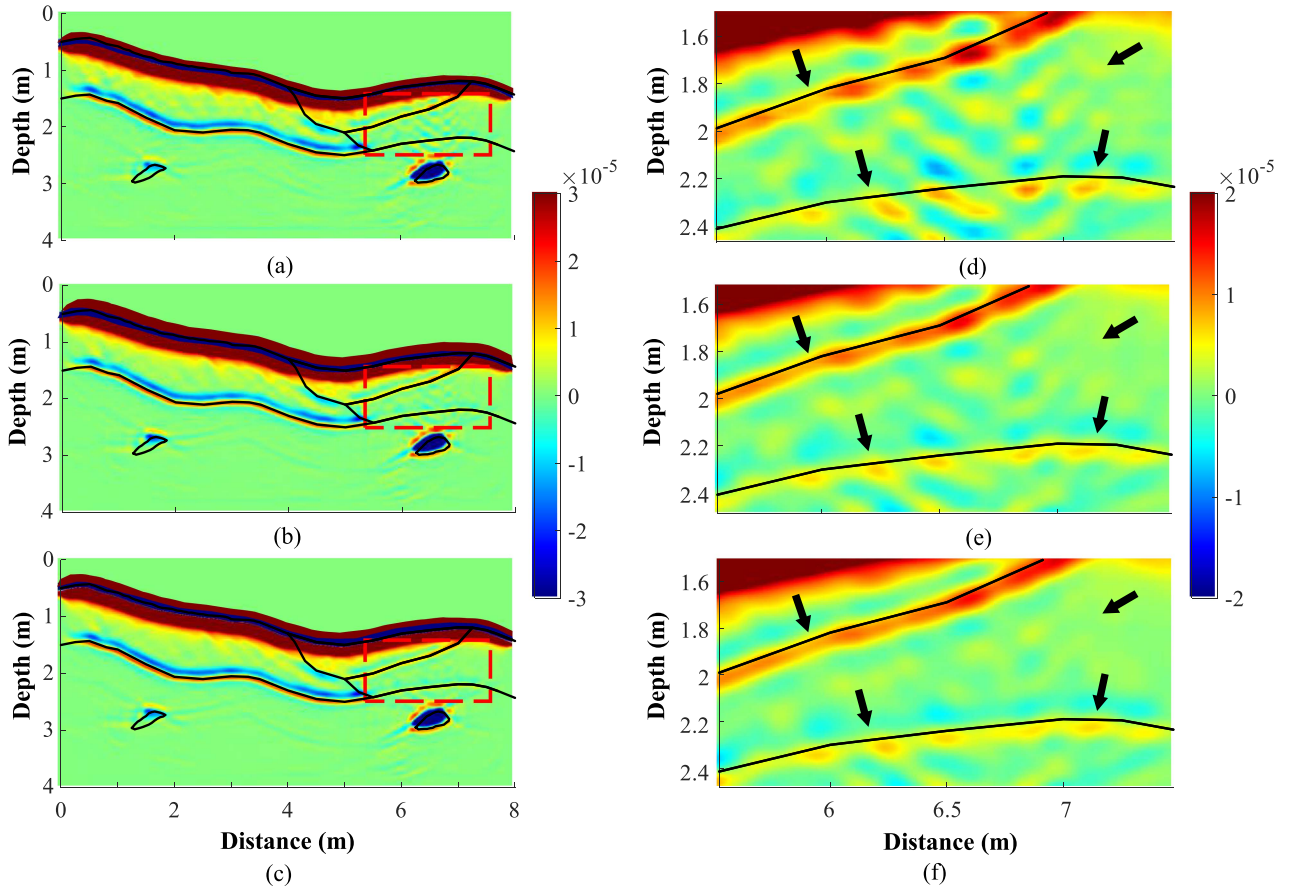


Fig. 12. RTM imaging results of different orders. (a) $P = 4$, (b) $P = 6$, (c) $P = 8$, (d), (e), and (f) are local enlargement of (a), (b), and (c).

to some extent due to the influence of undulating topography and irregular shape.

The simulation results of the wide-angle method for the model are considered. The transmitting antenna is placed in the center of the simulation area, and the receiving antennas are placed on both sides of the transmitting antenna along the undulating topography, and a total of 165 waveforms are recorded. The simulation window length is 70 ns, the excitation source is still a 200-MHz zero-phase Ricker wavelet, and the excitation source is 0.1-m away from the ground surface. With the same CFS-PML absorption boundary, Fig. 11(b) is the forward profile received by the wide-angle method.

In Fig. 11(b), due to a certain distance between the antenna and the surface, the reflection interface between direct waves in the air and the surface is clearly visible, but it cannot reflect the real form of the underground interface and anomalies. In the depth of 20–40 ns, the reflection waveform with strong energy on the left can be seen, which is the interface of the underground interface. At about 45 ns, there are two hyperbolic reflection waveforms on the left and right, and the energy intensity characteristics are the same as those in the profile method.

In order to verify the practicability of this algorithm, the SETD simulation results above are migrated in reverse time, the zero-time imaging condition is adopted, and the orders are set as 4, 6, and 8, respectively, to obtain the following diagrams. As can be seen from Fig. 12, with the increase of the order,

the shape and position of the undulating interface becomes clearer, the clutter signal becomes weaker, the details of the model become more prominent, and the anomalous body is well delineated. The clutter in the center area of Fig. 12(f) is significantly reduced compared with that in Fig. 12(d) and (e). The interface morphology at the top and bottom of Fig. 12(d) is not clear, with breakpoints, which cannot truly reflect the details of the model. However, in Fig. 12(e), especially in Fig. 12(f), these two interfaces' morphology are clear, and the clutter is greatly reduced. It can be seen that with the increase of SETD order, the imaging effect of RTM is also significantly improved. Therefore, the RTM imaging results based on SETD well verify the great potential of this method in the migration.

VI. CONCLUSION

In this article, we propose an SETD forward algorithm for GPR based on CFS-PML and per-element GPU parallel framework. The CFS-PML equation was derived by an ADE strategy and promoted to the second-order electromagnetic wave equation. Specifically, to effectively improve the stability of the algorithm, we derived the SETD matrix equation according to the 2-D TM electromagnetic wave equation with the CFS-PML boundary, and used the central difference method to discretize the time domain. Moreover, to effectively raise

computing performance and save storage space, we adopted the per-element SETD forward strategy with GPU parallel acceleration.

Three groups of experiments first conducted the rational use of our algorithm as follows: 1) Taking a long and narrow model as an example, the appropriate selection of the key parameters m , R , κ , and α in the CFS-PML under different orders was discussed in detail. Meanwhile, an additional conclusion is that compared with FETD, the number of CFS-PML layers of SETD is less, which shows the advantage of high computational efficiency. 2) Taking a simple model as an example, the convergence analysis experiment on the spatial-step ds was carried out. The analysis results verified the higher accuracy and calculation speed of SETD than the fine grid FETD. 3) Taking a simple model without the CFS-PML as an example, we compared the calculation time and speed-up ratio of GPU parallel algorithm and CPU serial algorithm combined with the per-element strategy at different orders. The results showed that the computing performance is effectively improved. Then, the numerical simulation and RTM algorithm of per-element GPU parallel SETD algorithm based on CFS-PML was accomplished and expectedly applied to a complex undulating surface geoelectric model. The experiments' results showed that: the SETD well simulated the model with complex physical parameter distribution, and the RTM imaging well fit the irregular terrain and irregular anomalies. Moreover, with the increase of the SETD order, the clutter signal gradually decreased, the model details were more prominent, and the imaging quality was significantly improved.

In summary, the comparison results of this article fully proved the SETD algorithm has great potential in RTM imaging. It makes us believe that this algorithm is especially suited for numerical simulation and RTM of GPR, which has a better guiding significance for the further work of underground structure exploration.

APPENDIX

The expansions of the coordinate stretching variables in PML are as follows:

$$\begin{cases} (j\omega)^2 s_x s_y = (j\omega)^2 \kappa_x \kappa_y + j\omega (\kappa_y \beta_x + \kappa_x \beta_y) + \beta_x \beta_y \\ \quad - \kappa_y \alpha_x \beta_x - \kappa_x \alpha_y \beta_y + S_x \frac{1}{\alpha_x + j\omega} + S_y \frac{1}{\alpha_y + j\omega} \\ \frac{s_y}{s_x} = \frac{\kappa_y}{\kappa_x} + T_x \frac{1}{\alpha_y + j\omega} - R_x \frac{1}{j\omega + \beta_x / \kappa_x + \alpha_x} \\ \frac{s_x}{s_y} = \frac{\kappa_x}{\kappa_y} + T_y \frac{1}{\alpha_x + j\omega} - R_y \frac{1}{j\omega + \beta_y / \kappa_y + \alpha_y} \end{cases} \quad (18)$$

The auxiliary variables in the formula are as follows:

$$\begin{cases} T_x = \frac{(\alpha_x - \alpha_y) \beta_y}{[\beta_x + \kappa_x (\alpha_x - \alpha_y)]}, T_y = \frac{(\alpha_y - \alpha_x) \beta_x}{[\beta_y + \kappa_y (\alpha_y - \alpha_x)]} \\ R_x = \frac{\beta_x [\kappa_x \kappa_y (\alpha_x - \alpha_y) + \kappa_y \beta_x - \kappa_x \beta_y]}{\kappa_x^2 [\beta_x + \kappa_x (\alpha_x - \alpha_y)]} \\ R_y = \frac{\beta_y [\kappa_x \kappa_y (\alpha_y - \alpha_x) + \kappa_x \beta_y - \kappa_y \beta_x]}{\kappa_y^2 [\beta_y + \kappa_y (\alpha_y - \alpha_x)]} \\ S_x = \alpha_x^2 \beta_x \kappa_y - \frac{\alpha_x^2 \beta_x \beta_y}{\alpha_x - \alpha_y}, S_y = -\alpha_y^2 \beta_y \kappa_x - \frac{\alpha_y^2 \beta_y \beta_x}{\alpha_y - \alpha_x} \end{cases} \quad (19)$$

The relation of auxiliary fields P and Q in (3) is obtained as follows:

$$\begin{cases} (\alpha_y + j\omega) P_{1x} = T_x \frac{\partial E_z}{\partial x} \\ (\alpha_x + j\omega) P_{1y} = T_y \frac{\partial E_z}{\partial y} \\ (j\omega + \beta_x / \kappa_x + \alpha_x) P_{2x} = R_x \frac{\partial E_z}{\partial x} \\ (j\omega + \beta_y / \kappa_y + \alpha_y) P_{2y} = R_y \frac{\partial E_z}{\partial y} \\ (\alpha_x + j\omega) Q_x = \varepsilon S_x E_z \\ (\alpha_y + j\omega) Q_y = \varepsilon S_y E_z \end{cases} \quad (20)$$

And convert it to the time domain available

$$\begin{cases} \alpha_y P_{1x} + \frac{\partial P_{1x}}{\partial t} = T_x \frac{\partial E_z}{\partial x} \\ (\beta_x / \kappa_x + \alpha_x) P_{2x} + \frac{\partial P_{2x}}{\partial t} = R_x \frac{\partial E_z}{\partial x} \\ \alpha_x P_{1y} + \frac{\partial P_{1y}}{\partial t} = T_y \frac{\partial E_z}{\partial y} \\ (\beta_y / \kappa_y + \alpha_y) P_{2y} + \frac{\partial P_{2y}}{\partial t} = R_y \frac{\partial E_z}{\partial y} \\ \alpha_x Q_x + \frac{\partial Q_x}{\partial t} = \varepsilon S_x E_z \\ \alpha_y Q_y + \frac{\partial Q_y}{\partial t} = \varepsilon S_y E_z \end{cases} \quad (21)$$

The Galerkin weighted residual method was used to discretize the above equation

$$\begin{cases} \alpha_y \iint_{\Omega} P_{1x} v d\Omega + \iint_{\Omega} \frac{\partial P_{1x}}{\partial t} v d\Omega = T_x \iint_{\Omega} \frac{\partial E_z}{\partial x} v d\Omega \\ (\beta_x / \kappa_x + \alpha_x) \iint_{\Omega} P_{2x} v d\Omega + \iint_{\Omega} \frac{\partial P_{2x}}{\partial t} v d\Omega = R_x \iint_{\Omega} \frac{\partial E_z}{\partial x} v d\Omega \\ \alpha_x \iint_{\Omega} P_{1y} v d\Omega + \iint_{\Omega} \frac{\partial P_{1y}}{\partial t} v d\Omega = T_y \iint_{\Omega} \frac{\partial E_z}{\partial y} v d\Omega \\ (\beta_y / \kappa_y + \alpha_y) \iint_{\Omega} P_{2y} v d\Omega + \iint_{\Omega} \frac{\partial P_{2y}}{\partial t} v d\Omega = R_y \iint_{\Omega} \frac{\partial E_z}{\partial y} v d\Omega \\ \alpha_x \iint_{\Omega} Q_x v d\Omega + \iint_{\Omega} \frac{\partial Q_x}{\partial t} v d\Omega = \varepsilon S_x \iint_{\Omega} E_z v d\Omega \\ \alpha_y \iint_{\Omega} Q_y v d\Omega + \iint_{\Omega} \frac{\partial Q_y}{\partial t} v d\Omega = \varepsilon S_y \iint_{\Omega} E_z v d\Omega \end{cases} \quad (22)$$

where Γ and Ω are the boundaries and the calculated region, respectively, and v is the trial function. The Dirichlet boundary condition with the displacement of 0 is adopted on the PML boundary, and the auxiliary field equation can be deduced by the Galerkin method

$$\begin{cases} C_{1x} P_{1x} + C \dot{P}_{1x} = B_1 E_z, & C_{2x} P_{2x} + C \dot{P}_{2x} = B_2 E_z \\ C_{1y} P_{1y} + C \dot{P}_{1y} = B_3 E_z, & C_{2y} P_{2y} + C \dot{P}_{2y} = B_4 E_z \\ C_{1y} Q_x + C \dot{Q}_x = B_5 E_z, & C_{1x} Q_y + C \dot{Q}_y = B_6 E_z \end{cases} \quad (23)$$

where the matrices are expressed as

$$\begin{cases} C_{1x} = \alpha_y C, C_{1y} = \alpha_x C \\ C_{2x} = (\beta_x / \kappa_x + \alpha_x) C, C_{2y} = (\beta_y / \kappa_y + \alpha_y) C \\ B_1 = \mu T_x K_x, B_2 = \mu R_x K_x, B_3 = \mu T_y K_y \\ B_4 = \mu R_y K_y, B_5 = \varepsilon S_x C, B_6 = \varepsilon S_y C \end{cases} \quad (24)$$

where N is the shape function selected in the calculation area

$$\begin{cases} \left(\frac{C_{1x}}{2} + \frac{C}{\Delta t} \right) P_{1x}^{n+1} + \left(\frac{C_{1x}}{2} - \frac{C}{\Delta t} \right) P_{1x}^{n-1} = B_1 E^n \\ \left(\frac{C_{2x}}{2} + \frac{C}{\Delta t} \right) P_{2x}^{n+1} + \left(\frac{C_{2x}}{2} - \frac{C}{\Delta t} \right) P_{2x}^{n-1} = B_2 E^n \\ \left(\frac{C_{1y}}{2} + \frac{C}{\Delta t} \right) P_{1y}^{n+1} + \left(\frac{C_{1y}}{2} - \frac{C}{\Delta t} \right) P_{1y}^{n-1} = B_3 E^n \\ \left(\frac{C_{2y}}{2} + \frac{C}{\Delta t} \right) P_{2y}^{n+1} + \left(\frac{C_{2y}}{2} - \frac{C}{\Delta t} \right) P_{2y}^{n-1} = B_4 E^n \\ \left(\frac{C_{1y}}{2} + \frac{C}{\Delta t} \right) Q_y^{n+1} + \left(\frac{C_{1y}}{2} - \frac{C}{\Delta t} \right) Q_y^{n-1} = B_5 E^n \\ \left(\frac{C_{1x}}{2} + \frac{C}{\Delta t} \right) Q_x^{n+1} + \left(\frac{C_{1x}}{2} - \frac{C}{\Delta t} \right) Q_x^{n-1} = B_6 E^n. \end{cases} \quad (25)$$

The above equation is the auxiliary field time discrete equation in the PML, and the field value at each time can be solved immediately when combined with (16).

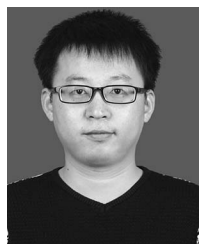
ACKNOWLEDGMENT

The authors would like to thank the Editors for providing helpful guidance to the implementation of this work, they are also grateful to the anonymous reviewers for their constructive comments and suggestions that help to improve the previous version of this paper.

REFERENCES

- [1] D. J. Daniels, *Ground Penetrating Radar*, 2nd ed. London, U.K.: IEE, 2004.
- [2] L. Zhang, Y. Xu, Z. Zeng, J. Li, and D. Zhang, "Simulation of Martian near-surface structure and imaging of future GPR data from Mars," *IEEE Trans. Geosci. Remote Sens.*, vol. 60, 2022, Art. no. 5101812.
- [3] D. Feng, C. Cao, and X. Wang, "Multiscale full-waveform dual-parameter inversion based on total variation regularization to on-ground GPR data," *IEEE Trans. Geosci. Remote Sens.*, vol. 57, no. 11, pp. 9450–9465, Nov. 2019.
- [4] D. Feng, T. Li, G. Li, and X. Wang, "Reverse time migration of GPR data based on accurate velocity estimation and artifacts removal using total variation de-noising," *J. Appl. Geophys.*, vol. 198, Mar. 2022, Art. no. 104563.
- [5] X. Lu, A. Song, R. Qian, and L. Liu, "Anisotropic reverse-time migration of ground-penetrating radar data collected on the sand dunes in the Badain Jaran Desert," *IEEE J. Sel. Topics Appl. Earth Observ. Remote Sens.*, vol. 11, no. 2, pp. 647–654, Feb. 2018.
- [6] K. Yee, "Numerical solution of initial boundary value problems involving Maxwell's equations in isotropic media," *IEEE Trans. Antennas Propag.*, vol. 14, no. 3, pp. 302–307, May 1966.
- [7] J. Li, Z. Zeng, L. Huang, and F. Liu, "GPR simulation based on complex frequency shifted recursive integration PML boundary of 3D high order FDTD," *Comput. Geosci.*, vol. 49, pp. 121–130, Dec. 2012.
- [8] I. Giannakis, A. Giannopoulos, and C. Warren, "A realistic FDTD numerical modeling framework of ground penetrating radar for landmine detection," *IEEE J. Sel. Topics Appl. Earth Observ. Remote Sens.*, vol. 9, no. 1, pp. 37–51, Aug. 2015.
- [9] J. Irving and R. Knight, "Numerical modeling of ground-penetrating radar in 2-D using MATLAB," *Comput. Geosci.*, vol. 32, no. 9, pp. 1247–1258, Nov. 2006.
- [10] N. J. Cassidy and T. M. Millington, "The application of finite-difference time-domain modelling for the assessment of GPR in magnetically lossy materials," *J. Appl. Geophys.*, vol. 67, no. 4, pp. 296–308, Apr. 2009.
- [11] D. Feng, L. Yang, and X. Wang, "The unsplit convolutional perfectly matched layer absorption performance analysis of evanescent wave in GPR FDTD forward modeling," *Chin. J. Geophys.*, vol. 59, no. 12, pp. 4733–4746, Dec. 2016.
- [12] A. Taflov, "Review of the formulation and applications of the finite-difference time-domain method for numerical modeling of electromagnetic wave interactions with arbitrary structures," *Wave Motion*, vol. 10, no. 6, pp. 547–582, Dec. 1988.
- [13] D. Feng and X. Wang, "Convolution perfectly matched layer for the finite-element time-domain method modeling of ground penetrating radar," *Chin. J. Geophys.*, vol. 60, no. 1, pp. 413–423, Jan. 2017.
- [14] D. Feng, S. Ding, and X. Wang, "An exact PML to truncate lattices with unstructured-mesh-based adaptive finite element method in frequency domain for ground penetrating radar simulation," *J. Appl. Geophys.*, vol. 170, Nov. 2019, Art. no. 103836.
- [15] X. Wang, D. Feng, D. Yang, and X. Wang, "An interpolating scaling functions method with low-storage five-stage fourth-order explicit Runge-Kutta schemes for 3D ground penetrating radar simulation," *J. Appl. Geophys.*, vol. 180, Sep. 2020, Art. no. 104128.
- [16] G. C. Cohen, *Higher-Order Numerical Methods for Transient Wave Equations*. Berlin, Germany: Springer, 2002.
- [17] D. Feng, X. Wang, and B. Zhang, "Specific evaluation of tunnel lining multi-defects by all-refined GPR simulation method using hybrid algorithm of FETD and FDTD," *Construction Building Materials*, vol. 185, pp. 220–229, Oct. 2018.
- [18] K. J. Burns et al., "Dedalus: A flexible framework for numerical simulations with spectral methods," *Phys. Rev.*, vol. 2, no. 2, Apr. 2020, Art. no. 023068.
- [19] A. T. Patera, "A spectral element method for fluid dynamics: Laminar flow in a channel expansion," *J. Comput. Phys.*, vol. 54, no. 3, pp. 468–488, Jun. 1984.
- [20] G. Seriani and E. Priolo, "Spectral element method for acoustic wave simulation in heterogeneous media," *Finite Elements Anal. Des.*, vol. 16, no. 3/4, pp. 337–348, Jun. 1994.
- [21] E. Priolo, J. M. Carcione, and G. Seriani, "Numerical simulation of interface waves by high-order spectral modeling techniques," *J. Acoustical Soc. Amer.*, vol. 95, no. 2, pp. 681–693, Jun. 1994.
- [22] D. Komatitsch, J. P. Vilotte, R. Vai, and M. Jose, "The spectral element method for elastic wave equations-Application to 2-D and 3-D seismic problems," *Int. J. Numer. Methods Eng.*, vol. 45, no. 9, pp. 1139–1164, Jun. 1999.
- [23] D. Komatitsch and J. Tromp, "Spectral-element simulations of global seismic wave Propagation-I. Validation," *Geophys. J. Int.*, vol. 149, no. 2, pp. 390–412, May 2002.
- [24] D. Komatitsch and J. Tromp, "Spectral-element simulations of global seismic wave propagation-II. 3-D models, oceans, rotation, and self-gravitation," *Geophys. J. Int.*, vol. 150, no. 1, pp. 303–318, Jul. 2002.
- [25] D. Komatitsch et al., "Simulations of ground motion in the Los Angeles basin based upon the spectral-element method," *Bull. Seismological Soc. Amer.*, vol. 94, no. 1, pp. 187–206, Feb. 2004.
- [26] D. Komatitsch, S. Tsuboi, and J. Tromp, "The spectral-element method in seismology," *Geophysical Monograph Ser.*, vol. 157., pp. 205–228, Jan. 2005.
- [27] J. H. Lee, T. Xiao, and Q. H. Liu, "A 3-D spectral-element method using mixed-order curl conforming vector basis functions for electromagnetic fields," *IEEE Trans. Microw. Theory Techn.*, vol. 54, no. 1, pp. 437–444, Jan. 2006.
- [28] J. H. Lee, J. Chen, and Q. H. Liu, "A 3-D discontinuous spectral element time-domain method for Maxwell's equations," *IEEE Trans. Antennas Propag.*, vol. 57, no. 9, pp. 2666–2674, Jul. 2009.
- [29] X. Huang et al., "3D anisotropic modeling and identification for airborne EM systems based on spectral-element method," *Appl. Geophys.*, vol. 14, no. 3, pp. 419–430, Oct. 2017.
- [30] S. Zarei, B. Oskooi, N. Amini, and A. R. Dalkhani, "2D spectral element modeling of GPR wave propagation in inhomogeneous media," *J. Appl. Geophys.*, vol. 133, pp. 92–97, Oct. 2016.
- [31] R. Clayton and B. Engquist, "Absorbing boundary conditions for acoustic and elastic wave equations," *Bull. Seismological Soc. Amer.*, vol. 67, no. 6, pp. 1529–1540, Dec. 1977.
- [32] J. P. Berenger, "A perfectly matched layer for the absorption of electromagnetic waves," *J. Comput. Phys.*, vol. 114, no. 2, pp. 185–200, Oct. 1994.
- [33] F. L. Teixeira, C. D. Moss, W. C. Chew, and J. A. Kong, "Split-field and anisotropic-medium PML-FDTD implementations for inhomogeneous media," *IEEE Trans. Microw. Theory Techn.*, vol. 50, no. 1, pp. 30–35, Jan. 2002.
- [34] J. F. Wang et al., "The split-field PML absorbing boundary condition for the unconditionally stable node-based LOD-RPIM method," *IEEE Antennas Wireless Propag. Lett.*, vol. 17, no. 10, pp. 1920–1924, Sep. 2018.
- [35] Z. S. Sacks, D. M. Kingsland, R. Lee, and J. F. Lee, "A perfectly matched anisotropic absorber for use as an absorbing boundary condition," *IEEE Trans. Antennas Propag.*, vol. 43, no. 12, pp. 1460–1463, Dec. 1995.
- [36] D. Correia and J. M. Jin, "Performance of regular PML, CFS-PML, and second-order PML for waveguide problems," *Microw. Opt. Technol. Lett.*, vol. 48, no. 10, pp. 2121–2126, Jul. 2006.

- [37] M. Kuzuoglu and R. Mittra, "Frequency dependence of the constitutive parameters of causal perfectly matched anisotropic absorbers," *IEEE Microw. Guided Wave Lett.*, vol. 6, no. 12, pp. 447–449, Dec. 1996.
- [38] J. P. Berenger, "Improved PML for the FDTD solution of wave-structure interaction problems," *IEEE Trans. Antennas Propag.*, vol. 45, no. 3, pp. 466–473, Mar. 1997.
- [39] J. P. Berenger, "Evanescence waves in PML's: Origin of the numerical reflection in wave-structure interaction problems," *IEEE Trans. Antennas Propag.*, vol. 47, no. 10, pp. 1497–1503, Oct. 1999.
- [40] J. P. Berenger, "Application of the CFS PML to the absorption of evanescent waves in waveguides," *IEEE Microw. Wireless Compon. Lett.*, vol. 12, no. 6, pp. 218–220, Jun. 2002.
- [41] M. Masoud and A. Abdolali, "Optimization of the perfectly matched layer for the finite-element time-domain method," *IEEE Microw. Wireless Compon. Lett.*, vol. 17, no. 1, pp. 10–12, Jan. 2007.
- [42] M. Masoud and A. Abdolali, "Complex frequency shifted-perfectly matched layer for the finite-element time-domain method," *AEU Int. J. Electron. Commun.*, vol. 63, pp. 72–77, Jan. 2009.
- [43] X. Ma, Y. Li, and J. Song, "A stable auxiliary differential equation perfectly matched layer condition combined with low-dispersive symplectic methods for solving second-order elastic wave equations," *Geophysics*, vol. 84, no. 4, pp. T193–T206, Jul. 2019.
- [44] C. S. Cho and M. K. Son, "Application of ADE-PML boundary condition to SEM using variational formulation of velocity-stress 3D wave equation," *Geophys. Geophysical Exploration*, vol. 15, no. 2, pp. 57–65, Mar. 2012.
- [45] X. Song, T. Liu, D. Xiang, and Y. Su, "GPR antipersonnel mine detection based on tensor robust principal analysis," *Remote Sens.*, vol. 11, no. 8, Apr. 2019, Art. no. 984.
- [46] D. Xiang, K. Zhou, and Y. Su, "Fast prescreening for GPR antipersonnel mine detection via go decomposition," *IEEE Geosci. Remote Sens. Lett.*, vol. 16, no. 1, pp. 15–19, Sep. 2018.
- [47] J. H. Bradford et al., "Reverse-time migration from rugged topography to image ground-penetrating radar data in complex environments," *Engineering*, vol. 4, no. 5, pp. 661–666, Sep. 2018.
- [48] H. Liu, Z. Long, F. Han, G. Fang, and Q. H. Liu, "Frequency-domain reverse-time migration of ground penetrating radar based on layered medium green's functions," *IEEE J. Sel. Topics Appl. Earth Observ. Remote Sens.*, vol. 11, no. 8, pp. 2957–2965, Jun. 2018.
- [49] A. Taflov and M. E. Brodwin, "Numerical solution of steady-state EM scattering problems using the time-dependent Maxwell's equations," *IEEE Trans. Microw. Theory Techn.*, vol. 23, no. 8, pp. 623–630, Aug. 1975.
- [50] Y. Liu, J. H. Lee, X. T., and Q. Liu, "A spectral-element time-domain solution of Maxwell's equations," *Microw. Opt. Technol. Lett.*, vol. 48, no. 4, pp. 673–680, Feb. 2006.
- [51] N. Liu, L. E. Tobón, Y. Zhao, Y. Tang, and Q. H. Liu, "Mixed spectral-element method for 3-D Maxwell's eigenvalue problem," *IEEE Trans. Microw. Theory Techn.*, vol. 63, no. 2, pp. 317–325, Feb. 2015.
- [52] Q. Ren, L. E. Tobon, Q. Sun, and Q. Liu, "A new 3-D nonspurious discontinuous galerkin spectral element time-domain (DG-SETD) method for maxwell's equations," *IEEE Trans. Antennas Propag.*, vol. 63, no. 6, pp. 2585–2594, Jun. 2015.
- [53] T. Sauer and Y. Xu, "On multivariate lagrange interpolation," *Math. Comp.*, vol. 64, no. 211, pp. 1147–1170, Jul. 1995.
- [54] C. Warren et al., "A CUDA-based GPU engine for grpMax: Open source FDTD electromagnetic simulation software," *Comput. Phys. Commun.*, vol. 237, pp. 208–218, Apr. 2019.



Xun Wang was born in Henan, China, in 1990. He received the B.S., M.S., and Ph.D. degrees in geophysics from Central South University, Changsha, China, in 2013, 2016, and 2020, respectively.

He is an Associate Professor with the School of Geosciences and Info-Physics, Central South University. His research interests include the simulation of electromagnetic waves and the full-waveform inversion of ground-penetrating radar data.

Dr. Wang is a Reviewer for IEEE GEOSCIENCE AND REMOTE SENSING LETTERS, *Remote Sensing*, and the

IEEE ACCESS.



Tianxiao Yu was born in Anhui, China, in 2001. He received the B.S. degree in geophysics, in 2022, from Central South University, Changsha, China, where he is currently working toward the M.S. degree in geological resources and geological engineering with the College of Geoscience and Info-Physics.

His research interests include the forward, migration, and inversion of ground penetrating radar data.



Deshan Feng received the B.S., M.S., and Ph.D. degrees in geophysics from Central South University, Changsha, China, in 2000, 2003, and 2006, respectively.

From 2013 to 2014, he was a Senior Visiting Scholar with the Department of Earth Science, Rice University, Houston, TX, USA. He is currently a Full Professor and the Director with the Department of Geophysics, School of Geosciences and Info-Physics, Central South University. His research interests include the simulation wavelet analysis of electromagnetic waves.

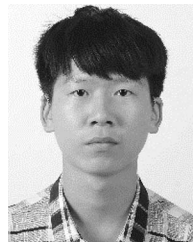
netic waves.

Dr. Feng is a Reviewer for IEEE TRANSACTIONS ON GEOSCIENCE AND REMOTE SENSING, *Computers & Geosciences*, *Geophysics*.



Siyuan Ding was born in Jiangsu Province, China, in 1995. She received the B.S. degree in prospecting technology and engineering from the China University of Petroleum, Qingdao, Shandong, China, in 2017, and the M.S. degree in geological resources and geological engineering from the College of Geosciences and Info-Physics, Central South University, Changsha, China, in 2020. She is currently working toward the Ph.D. degree in geological resources and geological engineering with the College of Geosciences and Info-Physics, Central South University.

Her research interests include the numerical simulation and inversion of ground penetrating radar data.



Bingchao Li was born in Henan, China, in 2000. He received the B.S. degree in geophysics, in 2022, from Central South University, Changsha, China, where he is currently working toward the Ph.D. degree in geological resources and geological engineering with the College of Geosciences and Info-Physics.

His research interests include forward and inversion of seismic and ground penetrating radar data.



Yuxin Liu was born in Hunan, China, in 2001. She received the B.S. degree in geophysics, in 2022, from Central South University, Changsha, China, where she is currently working toward the Ph.D. degree in geological resources and geological engineering with the College of Geosciences and Info-Physics.

Her research interests include the assessment and detection of tree trunk defects and inversion of ground penetrating radar data.



Zheng Feng was born in Hunan, China, in 2001. She received the B.S. degree in geophysics, in 2022, from Central South University, Changsha, China, where she is currently working toward the Ph.D. degree in geological resources and geological engineering with the College of Geosciences and Info-Physics.

Her research interests include GPR reverse time migration and the urban road disease detection.